Three-Dimensional Dual-Potential Procedure for Inlets and Indraft Wind Tunnels

K. V. Rao*
Iowa State University, Ames, Iowa
Joseph L. Steger†
NASA Ames Research Center, Moffett Field, California
and
R. H. Pletcher‡
Iowa State University, Ames, Iowa

A dual-potential decomposition of the velocity field into a scalar and a vector potential function is extended to three dimensions and used in the finite-difference simulation of steady three-dimensional inviscid rotational flow through ducts and inlets. The procedure has been used to simulate the flow through the 80 × 120 ft wind tunnel at NASA Ames Research Center. Vanes and screens located at the entrance of the inlet are modeled using actuator disk theory. The numerical predictions are in good agreement with experimental data.

Introduction

THERE has been an ongoing need to develop efficient computational procedures to simulate the inviscid but rotational flow through ducts and inlets in which turning vane losses and fan work can be modeled. Such a code can be used for the design of jet inlets, axial compressors, and wind tunnels in which a large number of flow simulations is needed to study the effects of different geometries and flow conditions. Inviscid rotational flow is governed by the Euler equations, and a very efficient numerical procedure has been developed for solving these equations for two-dimensional subsonic and transonic flow by decomposing the velocity field into a scalar potential and a vector potential field.[1,2] This will be referred to as a dual-potential decomposition. Besides running with the efficiency of transonic potential codes, the dual-potential formulation for solving the Euler equations permits entropy, total enthalpy, and measures of vorticity to be treated as dependent variables. Moreover, this formulation is very efficient for low-speed flow simulation. Related but not necessarily equivalent procedures are described elsewhere.[3-6]

In this work the dual-potential formulation of Refs. 1 and 2 is extended to three dimensions and is used for simulating indraft wind-tunnel flows. In particular, flow through the inlet of the 80 × 120 ft leg of the NASA Ames National Full-Scale Aerodynamics Complex (NFAC) is simulated using actuator-disk theory to model the inlet screens and flow-straightening vanes. The governing equations and velocity field decomposition are described in the next section, followed by a description of the numerical solution procedure. Numerical results obtained for the 80 × 120 ft leg of the NFAC are then compared with available data.

Presented as Paper 87-0598 at the AIAA 25th Aerospace Sciences Meeting, Reno, NV, Jan. 12-15, 1987; received March 2, 1987; revision received Aug. 19, 1988. This paper is declared a work of the U.S. Government and is not subject to copyright protection in the United States.

*Associate Scientist, Department of Mechanical Engineering. Member AIAA.
†Senior Staff Scientist, Fluid Dynamics Division. Associate Fellow AIAA.
‡Professor, Department of Mechanical Engineering. Member AIAA.

Three-Dimensional Dual Potential Formulation

Governing Equations in Primitive Variables

The governing equations of conservation of mass, momentum, and energy for a steady, inviscid flow that is adiabatic throughout (homenergic) can be represented as shown below.

Continuity:

$$\nabla \cdot \rho q = 0 \tag{1}$$

Crocco:

$$q \times \Omega = -T \nabla s \tag{2}$$

Bernoulli:

$$\frac{\rho}{\rho_r} = \left[1 - \frac{1}{2}\left(\frac{q^2}{h_r}\right)\right]^{1/(\gamma-1)} \exp[-(s - s_r)/R] \tag{3}$$

Convection of entropy:

$$q \cdot \nabla s = 0 \tag{4}$$

where ρ is the fluid density, u, v, and w are Cartesian velocity components, T is temperature, h is enthalpy, $q = (u,v,w)^T$, and s is entropy. Currently, total enthalpy is assumed to be constant. The subscript r denotes a reference state, and R is the perfect gas constant. The symbol ∇ represents the gradient operator. The vorticity vector Ω is defined as the curl of the velocity vector. Note that the entropy convection equation replaces a Crocco relation as it is formed by taking the dot product of the velocity vector with the Crocco equations.

Dual-Potential Velocity Decomposition

The velocity field can be expressed as the gradient of a scalar potential and the curl of a vector potential (cf. Ref. 7):

$$q = \nabla\phi + \nabla \times B; \qquad B = \begin{pmatrix} \vartheta \\ \chi \\ \psi \end{pmatrix} \tag{5}$$

so that

$$q = \begin{pmatrix} u \\ v \\ w \end{pmatrix} = \begin{pmatrix} \phi_x + \psi_y - \chi_z \\ \phi_y + \vartheta_z - \psi_x \\ \phi_z + \chi_x - \vartheta_y \end{pmatrix} \tag{6}$$

With this decomposition, the divergence of q is given by

$$\nabla \cdot q = \nabla^2 \phi \tag{7}$$

where ∇^2 is the Laplacian operator $\nabla \cdot \nabla$, and the curl (or vorticity) is given by

$$\Omega = \begin{pmatrix} w_y - v_z \\ u_z - w_x \\ v_x - u_y \end{pmatrix} = \begin{pmatrix} -(\vartheta_{yy} + \vartheta_{zz}) + (\chi_{xy} + \psi_{xz}) \\ -(\chi_{xx} + \chi_{zz}) + (\vartheta_{yx} + \psi_{yz}) \\ -(\psi_{xx} + \psi_{yy}) + (\vartheta_{xz} + \chi_{zy}) \end{pmatrix} \tag{8}$$

The three-dimensional velocity field is represented by four potential functions; thus, there is one degree of redundancy in this decomposition. Following Refs. 1 and 2, the scalar potential is retained in order to obtain an equation for ϕ that is similar to the transonic full-potential equation. A constraint is therefore imposed on the vector potential functions in order to uniquely specify the velocity field. A standard vector potential constraint that has often been employed (cf. Ref. 7) is the condition that the vector potential be divergence free, i.e.,

$$\nabla \cdot B = \vartheta_x + \chi_y + \psi_z = 0 \tag{9}$$

This consistency expression relates the vector potential functions to one another and removes the redundancy. It is used both to simplify the vorticity relations and to obtain an extra boundary condition (see also Refs. 3–5).

Subject to the consistency Eq. (9), the vorticity assumes the compact symmetric form

$$\nabla^2 B = -\Omega \tag{10}$$

An additional consistency equation relating the vorticities is obtained from the vector identity

$$\nabla \cdot \nabla \times q = \partial_x \Omega_1 + \partial_y \Omega_2 + \partial_z \Omega_3 = 0 \tag{11}$$

which is also the Laplacian operating on Eq. (9).

For the velocity decomposition given by Eq. (5), the continuity Eq. (1) now takes the form

$$(\rho\phi_x)_x + (\rho\phi_y)_y + (\rho\phi_z)_z = -[(\psi_y - \chi_z)\rho_x + (\vartheta_z - \psi_x)\rho_y + (\chi_x - \vartheta_y)\rho_z] \tag{12}$$

It may be noted that this differs from the usual form of the transonic full-potential equation by the presence of the nonzero right-hand-side terms describing the rotational component of the velocity. For constant density, Eq. (12) reduces simply to $\nabla^2 \phi = 0$.

Boundary Conditions

On any boundary surface two linear combinations of the vector potential functions can be kept constant, and the vector potential consistency relation, Eq. (9), can be used to solve for a third linear combination. Tangency is then imposed on a body boundary surface from

$$n \cdot \nabla \phi = -n \cdot \nabla \times B \tag{13}$$

In Cartesian coordinates, two components of B can be chosen to be constant on an x, y, or z boundary plane so that $n \cdot \nabla \times B = 0$ and $\nabla \cdot B = 0$ supplies a Neumann boundary condition for the third component. For example, on a $z =$ constant plane, ϑ and χ are taken as constants. Then ϑ_x and $\chi_y = 0$ and consistency gives $\psi_z = 0$, from which ψ can be determined on the $z =$ constant surface. Likewise, χ_x and $\vartheta_y = 0$ and tangency, $w = 0$, is satisfied by setting $\phi_z = 0$.

Generalized Curvilinear Coordinates

To simplify the treatment of arbitrary body boundaries in the numerical simulation, body-fitted curvilinear coordinates are employed, and the flow domain is mapped to a uniformly spaced rectangular coordinate region. The general coordinate transformation is defined by

$$\xi = \xi(x,y,z), \quad \eta = \eta(x,y,z), \quad \zeta = \zeta(x,y,z) \tag{14}$$

In terms of the independent variables ξ,η,ζ the Cartesian velocity components can be evaluated from the potential functions using the chain rule of partial differentiation on Eq. (6) as

$$u = (\xi_x\phi_\xi + \eta_x\phi_\eta + \zeta_x\phi_\zeta) + (\xi_y\psi_\xi + \eta_y\psi_\eta + \zeta_y\psi_\zeta) - (\xi_z\chi_\xi + \eta_z\chi_\eta + \zeta_z\chi_\zeta) \tag{15a}$$

$$v = (\xi_y\phi_\xi + \eta_y\phi_\eta + \zeta_y\phi_\zeta) + (\xi_z\vartheta_\xi + \eta_z\vartheta_\eta + \eta_z\vartheta_\zeta) - (\xi_x\psi_\xi + \eta_x\psi_\eta + \zeta_x\psi_\zeta) \tag{15b}$$

$$w = (\xi_z\phi_\xi + \eta_z\phi_\eta + \zeta_z\phi_\zeta) + (\xi_x\chi_\xi + \eta_x\chi_\eta + \zeta_x\chi_\zeta) - (\xi_y\vartheta_\xi + \eta_y\vartheta_\eta + \zeta_y\vartheta_\zeta) \tag{15c}$$

where the metric quantities used in the transformations in Eqs. (15) are defined in the usual way. Unscaled contravariant velocity components of the velocity vector q can be defined as

$$U = \xi_x u + \xi_y v + \xi_z w \tag{16a}$$

$$V = \eta_x u + \eta_y v + \eta_z w \tag{16b}$$

$$W = \zeta_x u + \zeta_y v + \zeta_z w \tag{16c}$$

The contravariant velocity components are conveniently split between the scalar potential contribution and the vector potential contribution as

$$U = U^\phi + U^B$$

$$V = V^\phi + V^B$$

$$W = W^\phi + W^B$$

where

$$U^\phi = A^{\xi\xi}\phi_\xi + A^{\xi\eta}\phi_\eta + A^{\xi\zeta}\phi_\zeta \tag{17a}$$

$$V^\phi = A^{\xi\eta}\phi_\xi + A^{\eta\eta}\phi_\eta + A^{\eta\zeta}\phi_\zeta \tag{17b}$$

$$W^\phi = A^{\xi\zeta}\phi_\xi + A^{\eta\zeta}\phi_\eta + A^{\zeta\zeta}\phi_\zeta \tag{17c}$$

$$U^B = (\nabla\xi \times \nabla\eta) \cdot B_\eta + (\nabla\xi \times \nabla\zeta) \cdot B_\zeta \tag{17d}$$

$$V^B = (\nabla\eta \times \nabla\xi) \cdot B_\xi + (\nabla\eta \times \nabla\zeta) \cdot B_\zeta \tag{17e}$$

$$W^B = (\nabla\zeta \times \nabla\xi) \cdot B_\xi + (\nabla\zeta \times \nabla\eta) \cdot B_\eta \tag{17f}$$

and

$$A^{\xi\xi} = \nabla\xi \cdot \nabla\xi = \xi_x^2 + \xi_y^2 + \xi_z^2$$

$$A^{\eta\eta} = \nabla\eta \cdot \nabla\eta = \eta_x^2 + \eta_y^2 + \eta_z^2$$

$$A^{\zeta\zeta} = \nabla\zeta \cdot \nabla\zeta = \zeta_x^2 + \zeta_y^2 + \zeta_z^2$$

$$A^{\xi\eta} = \nabla\xi \cdot \nabla\eta = \xi_x\eta_x + \xi_y\eta_y + \xi_z\eta_z$$

$$A^{\xi\zeta} = \nabla\xi \cdot \nabla\zeta = \xi_x\zeta_x + \xi_y\zeta_y + \xi_z\zeta_z$$

$$A^{\eta\zeta} = \nabla\eta \cdot \nabla\zeta = \eta_x\zeta_x + \eta_y\zeta_y + \eta_z\zeta_z$$

Governing Equations in Transformed Coordinates

The continuity Eq. (12) can now be written in transformed coordinates as

$$\left[\frac{\rho(A^{\xi\xi}\phi_\xi + A^{\xi\eta}\phi_\eta + A^{\xi\zeta}\phi_\zeta)}{J}\right]_\xi + \left[\frac{\rho(A^{\xi\eta}\phi_\xi + A^{\eta\eta}\phi_\eta + A^{\eta\zeta}\phi_\zeta)}{J}\right]_\eta + \left[\frac{\rho(A^{\xi\zeta}\phi_\xi + A^{\eta\zeta}\phi_\eta + A^{\zeta\zeta}\phi_\zeta)}{J}\right]_\zeta = -\left[\left(\frac{U^B}{J}\right)\rho_\xi + \left(\frac{V^B}{J}\right)\rho_\eta + \left(\frac{W^B}{J}\right)\rho_\zeta\right] \tag{18}$$

The Poisson equations for the vector potential functions can be transformed similarly employing the same metric groupings and can be written in a compact vector form as

$$\left(\frac{A^{\xi\xi}\boldsymbol{B}_\xi + A^{\xi\eta}\boldsymbol{B}_\eta + A^{\xi\zeta}\boldsymbol{B}_\zeta}{J}\right)_\xi + \left(\frac{A^{\xi\eta}\boldsymbol{B}_\xi + A^{\eta\eta}\boldsymbol{B}_\eta + A^{\eta\zeta}\boldsymbol{B}_\zeta}{J}\right)_\eta + \left(\frac{A^{\xi\zeta}\boldsymbol{B}_\xi + A^{\eta\zeta}\boldsymbol{B}_\eta + A^{\zeta\zeta}\boldsymbol{B}_\zeta}{J}\right)_\zeta = -\frac{\boldsymbol{\Omega}}{J} \tag{19}$$

In the same transformed coordinates, the Crocco relations are given as

$$v\Omega_3 - w\Omega_2 = -T(\xi_x s_\xi + \eta_x s_\eta + \zeta_x s_\zeta) \tag{20a}$$

$$w\Omega_1 - u\Omega_3 = -T(\xi_y s_\xi + \eta_y s_\eta + \zeta_y s_\zeta) \tag{20b}$$

$$u\Omega_2 - v\Omega_1 = -T(\xi_z s_\xi + \eta_z s_\eta + \zeta_z s_\zeta) \tag{20c}$$

and the entropy convection equation is given as

$$Us_\xi + Vs_\eta + Ws_\zeta = 0 \tag{21}$$

The consistency equation for the vector potential functions takes the form

$$\nabla \cdot \boldsymbol{B} = \nabla\xi \cdot \boldsymbol{B}_\xi + \nabla\eta \cdot \boldsymbol{B}_\eta + \nabla\zeta \cdot \boldsymbol{B}_\zeta = 0 \tag{22}$$

Similarly, the vorticity consistency Eq. (11) can be expressed as

$$\nabla \cdot \boldsymbol{\Omega} = \nabla\xi \cdot \boldsymbol{\Omega}_\xi + \nabla\eta \cdot \boldsymbol{\Omega}_\eta + \nabla\zeta \cdot \boldsymbol{\Omega}_\zeta = 0 \tag{23}$$

Solution Procedure

The dual-potential formulation outlined in the previous sections has several advantages. In an iterative solution scheme the governing Eqs. (18–21) are weakly coupled and hence can be solved separately, as described below. Because of the uncoupling, efficient solution schemes can be used for solving each individual equation. The rotational and irrotational components of velocity are also decoupled. As a result, the vector potential functions need be solved for only in the rotational part of the flow domain.

Because the equations are weakly coupled, an efficient iterative solution procedure can be used with each equation updated sequentially. At each grid point an initial guess is made for values of ϕ, ϑ, χ, ψ, s, and ρ, and for Ω_1, Ω_2, and Ω_3. The following iteration scheme is then implemented:

1) Vector potential functions ϑ, χ, and ψ. Using an implicit approximate factorization (AF) finite-difference method (ADI-like), individually update ϑ, χ, and ψ from the Poisson equations given by Eq. (19) for assumed values of Ω_1, Ω_2, and Ω_3. Boundary conditions for these equations are kept compatible with the consistency relation [Eq. (22)].

2) Scalar potential function ϕ. Update ϕ from the continuity Eq. (18) using an ADI-like algorithm for the transonic full-potential function and previously updated values of ϑ, χ, and ψ.

3) Entropy s. Using updated values of ϑ, χ, ψ, and ϕ, evaluate U, V, and W and update s from the convection Eq. (21). A partially upwind implicit AF finite-difference algorithm is used.

4) Density ρ. Update density from the Bernoulli Eq. (3), using previously updated values of u, v, w, and s.

5) Vorticities Ω_1, Ω_2, and Ω_3. Vorticity components are evaluated from Crocco's equations and the consistency relation for vorticity. Assuming $u > |v|$ and $|w|$ and $u \neq 0$, Ω_2 and Ω_3 are evaluated from Eqs. (20) as

$$\Omega_2 = [v\Omega_1 - T(\xi_z s_\xi + \eta_z s_\eta + \zeta_z s_\zeta)]/u \tag{24a}$$

$$\Omega_3 = [w\Omega_1 + T(\xi_y s_\xi + \eta_y s_\eta + \zeta_y s_\zeta)]/u \tag{24b}$$

and Ω_1 is determined from the vorticity consistency relation [Eq. (23)].

6) Test for convergence and, if necessary, return to step 1.

Numerical Algorithms

The numerical algorithms for Eqs. (18–23) are described in this section using the following notation. In the uniform computational domain we set $\Delta\xi = \Delta\eta = \Delta\zeta = 1$. The operator δ generally represents a central differencing; δ^b denotes a backward differencing, generally three-point second-order backward; δ^f denotes a forward differencing; and $\bar{\delta}$ represents the midpoint central-difference operator, i.e., $\bar{\delta}_\xi = [(\ )_{j+1/2} - (\ )_{j-1/2}]/\Delta\xi$. The conventional difference operators ∇ and Δ have their usual definitions, i.e., $\nabla = I - E^{-1}$ and $\Delta = E - I$, where E is the shifting operator, $Eu_j = u_{j+1}$, $E^{-1}u_j = u_{j-1}$. The indices j, k, and l refer to grid points in the ξ, η, and ζ directions, respectively. Generally a subscript is not shown unless it varies; for example, $u_{k+1} = u_{j,k+1,l}$.

ADI Algorithm for the Continuity and Poisson Equations

The continuity equation for ϕ, Eq. (18), is updated using an approximate factorization (ADI-type) algorithm in delta form. The steady-state form of the one described in Ref. 8 is used, and details can be found there. The differencing scheme, in AF form, is given by

$$[I - h\bar{\delta}_\xi(\hat{\rho}A^{\xi\xi})^n\bar{\delta}_\xi][I - h\bar{\delta}_\eta(\hat{\rho}A^{\eta\eta})^n\bar{\delta}_\eta][I - h\bar{\delta}_\zeta(\hat{\rho}A^{\zeta\zeta})^n\bar{\delta}_\zeta] \times (\phi^{n+1} - \phi^n) = h\omega[\bar{\delta}_\xi(\hat{\rho}U^\phi)^n + \bar{\delta}_\eta(\hat{\rho}V^\phi)^n + \bar{\delta}_\zeta(\hat{\rho}W^\phi)^n + (U^B/J)\delta_\xi\rho + (V^B/J)\delta_\eta\rho + (W^B/J)\delta_\zeta\rho - R_\infty] \tag{25}$$

where $\hat{\rho} = \rho/J$, and the superscript n refers to the iteration level. The differencing of the contravariant velocity component terms that appear on the right-hand side of Eq. (25) is

illustrated by considering U^{ϕ} and U^{B}. Central differencing in space is used throughout, except for ϕ terms, which are associated with a second derivative in ξ. Thus,

$$U^{\phi}_{j+1/2} = A^{\xi\xi}_{j+1/2}\,\Delta_{\xi}\phi_j + \tfrac{1}{2}(A^{\xi\eta}_{j+1}\delta_{\eta}\phi_{j+1} + A^{\xi\eta}_{j}\delta_{\eta}\phi_j) + \tfrac{1}{2}(A^{\xi\zeta}_{j+1}\delta_{\zeta}\phi_{j+1} + A^{\xi\zeta}_{j}\delta_{\zeta}\phi_j)$$

and

$$U^{B} = \xi_x u^{B} + \xi_y v^{B} + \xi_z w^{B}$$

where

$$u^{B} = (\xi_y\delta_{\xi}\psi + \eta_y\delta_{\eta}\psi + \zeta_y\delta_{\zeta}\psi) - (\xi_z\delta_{\xi}\chi + \eta_z\delta_{\eta}\chi + \zeta_z\delta_{\zeta}\chi)$$

$$v^{B} = (\xi_z\delta_{\xi}\vartheta + \eta_z\delta_{\eta}\vartheta + \zeta_z\delta_{\zeta}\vartheta) - (\xi_x\delta_{\xi}\psi + \eta_x\delta_{\eta}\psi + \zeta_x\delta_{\zeta}\psi)$$

$$w^{B} = (\xi_x\delta_{\xi}\chi + \eta_x\delta_{\eta}\chi + \zeta_x\delta_{\zeta}\chi) - (\xi_y\delta_{\xi}\vartheta + \eta_y\delta_{\eta}\vartheta + \zeta_y\delta_{\zeta}\vartheta)$$

The V and W terms are also treated with central differencing except for ϕ terms associated with second derivatives in η alone and ζ alone, respectively. In regions of supersonic flow, an upwind bias is used for ρ (cf. Ref. 8).

The freestream subtraction term R_{∞}, appearing in the right-hand side of Eq. (25), accounts for incomplete metric cancellation[8] and is given by

$$R_{\infty} = \bar{\delta}_{\xi}\left(\frac{\rho_{\infty}U_{\infty}}{J}\right) + \bar{\delta}_{\eta}\left(\frac{\rho_{\infty}V_{\infty}}{J}\right) + \bar{\delta}_{\zeta}\left(\frac{\rho_{\infty}W_{\infty}}{J}\right) \tag{26}$$

An ADI algorithm is used to solve Eq. (25). Rewriting Eq. (25) in the form

$$L_{\xi}L_{\eta}L_{\zeta}(\phi^{n+1} - \phi^{n}) = R \tag{27}$$

the ADI algorithm is implemented in three steps as

$$L_{\xi}\Delta\phi^{*} = R \tag{28a}$$

$$L_{\eta}\Delta\phi^{**} = \Delta\phi^{*} \tag{28b}$$

$$L_{\zeta}\Delta\phi^{n+1} = \Delta\phi^{**} \tag{28c}$$

$$\phi^{n+1} = \phi^{n} + \Delta\phi^{n} \tag{28d}$$

The algorithm given by Eqs. (28) requires only a series of scalar, tridiagonal inversions and is therefore solved efficiently. The relaxation parameter h, which appears in Eq. (25), is determined from a geometric sequence.[9] A second overrelaxation parameter ω is used to scale the residual.

Each of the Poisson equations for the vector potential functions is updated in a similar manner.

Convection Differencing and Relaxation

The differencing used with the convection equation is illustrated by considering the entropy convection equation in general coordinates:

$$Us_{\xi} + Vs_{\eta} + Ws_{\zeta} = 0 \tag{29}$$

Assuming U is generally larger than V and W, three-point, second-order-accurate central differencing is used in η and ζ, and three-point, second-order-accurate upwind differencing is used in ξ. Upwind differencing of Us_{ξ} is automatically achieved using

$$Us_{\xi} = U^{+}\delta^{b}_{\xi}s + U^{-}\delta^{f}_{\xi}s$$

where

$$U^{+} = \frac{U + |U|}{2} \quad \text{and} \quad U^{-} = \frac{U - |U|}{2}$$

The convection equation is then solved using the AF relaxation algorithm:

$$\begin{aligned}(I + hU^{+}\delta^{b}_{\xi} + hW\delta_{\zeta} - 3h|W|\Delta\nabla|_{\zeta})&\\ \times (I + hU^{-}\delta^{f}_{\xi} + hV\delta_{\eta} - 3h|V|\Delta\nabla|_{\eta})(s^{n+1} - s^{n})&\\ = -h[U^{+}\delta^{b}_{\xi} + U^{-}\delta^{f}_{\xi} + V\delta_{\eta} + W\delta_{\zeta}&\\ + |V|(\Delta\nabla)^{2}|_{\eta} + |W|(\Delta\nabla)^{2}|_{\zeta}]s^{n}&\end{aligned} \tag{30}$$

where h is another relaxation parameter ($h > 0$). Because central differencing is used in the η and ζ directions, numerical dissipation terms have been added to the differencing scheme.

Integration Algorithm for Vorticity and Consistency Boundary Condition

The consistency relation for vorticity, Eq. (23), is used to integrate Ω_1 in the ξ direction from an upstream boundary. Equation (23) can be represented in the form

$$a_1 f_{\xi} + a_2 f_{\eta} + a_3 f_{\zeta} = a_4 \tag{31}$$

where $f = \Omega_1$, $a_1 = \xi_x$, $a_2 = \eta_x$, $a_3 = \zeta_x$, and a_4 contains the remaining terms of Eq. (23).

Consider differencing this equation on a j plane using first-order one-sided differencing in ξ and central differencing in η and ζ. That is, at the jth plane

$$a_1(f_j - f_{j-1}) + a_2\frac{(f_{k+1} - f_{k-1})}{2}\Big|_j + a_3\frac{(f_{l+1} - f_{l-1})}{2}\Big|_j = a_4$$

Putting into the delta form, $f_j - f_{j-1}$, dividing by a_1, and approximately factoring, this difference equation is written as

$$\left(I + \frac{a_2}{a_1}\delta_{\eta}\right)\left(I + \frac{a_3}{a_1}\delta_{\zeta}\right)(f_j - f_{j-1}) = \frac{a_4}{a_1} - \left(\frac{a_2}{a_1}\delta_{\eta} + \frac{a_3}{a_1}\delta_{\zeta}\right)f_{j-1} \tag{32}$$

If three-point, second-order forward differencing is used for f_{ξ}, this becomes

$$\left(I + \frac{2a_2}{3a_1}\delta_{\eta}\right)\left(I + \frac{2a_3}{3a_1}\delta_{\zeta}\right)(f_j - f_{j-1}) = \frac{2}{3}\frac{a_4}{a_1} + \frac{1}{3}(f_{j-1} - f_{j-2}) - \frac{2}{3}\left(\frac{a_2}{a_1}\delta_{\eta} + \frac{a_3}{a_1}\delta_{\zeta}\right)f_{j-1} \tag{33}$$

Note that this approximate factorization is using a space delta, not an iteration delta. First-order backward differencing is used at the first ξ = constant plane, and second-order differencing is used at all successive planes to integrate the consistency relation for Ω_1. At each ξ plane the algorithm requires a series of simple tridiagonal inversions in η and ζ.

The consistency relation for the vector potential functions can be represented in the form given by Eq. (31) and is implemented at boundary surfaces by a procedure similar to the one described above.

Tangency Boundary Condition

Tangency or no-flow-through is imposed on a boundary surface by setting the appropriate contravariant velocity component to zero. On a ζ = constant plane, W is set to zero.

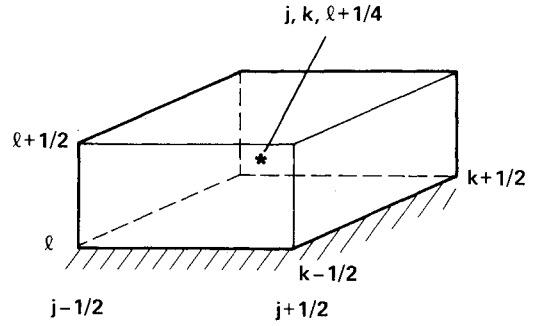

Fig. 1 Finite-difference cell near a wall boundary.

Tangency is enforced through implicit boundary conditions on ϕ, which are obtained by solving the continuity equation at the half-cells neighboring a solid boundary. The procedure is illustrated by considering a finite-difference cell (Fig. 1).

The center of the cell is located at $(j,k,l+\frac{1}{4})$. The finite-difference form of Eq. (18) can be written as

$$\left[\frac{(\hat{\rho}U)_{j+1/2,k,l+1/4}-(\hat{\rho}U)_{j-1/2,k,l+1/4}}{\Delta\xi}\right] + \left[\frac{(\hat{\rho}V)_{j,k+1/2,l+1/4}-(\hat{\rho}V)_{j,k-1/2,l+1/4}}{\Delta\eta}\right] + \left[\frac{(\hat{\rho}W)_{j,k,l+1/2}-(\hat{\rho}W^0)_{j,k,l}}{\Delta\zeta/2}\right]=0 \tag{34}$$

Evaluating variables at $l+\frac{1}{4}$ by weighted averaging between l and $l+1$, as, for example,

$$U_{j+1/2,k,l+1/4} = \tfrac{3}{4}U_{j+1/2,k,l} + \tfrac{1}{4}U_{j+1/2,k,l+1} = (I+\tfrac{1}{4}\Delta_\zeta)U_{j+1/2,k,l}$$

where

$$U_{j+1/2,k,l} = A^{\xi\xi}_{j+1/2}\Delta_\xi\phi_j + \tfrac{1}{2}(A^{\xi\eta}_{j+1}\delta_\eta\phi_{j+1} + A^{\xi\eta}_{j}\delta_\eta\phi_j) + \tfrac{1}{2}(A^{\xi\zeta}_{j+1}\Delta_\zeta\phi_{j+1} + A^{\xi\zeta}_{j}\Delta_\zeta\phi_j) + \text{vector potential terms}$$

To facilitate the application of approximate factorization, the cross derivative terms lag in time in the usual way to obtain the relaxation algorithm

$$[I-h\bar{\delta}_\xi(\hat{\rho}A^{\xi\xi})^n\bar{\delta}_\xi]\,[I-h\bar{\delta}_\eta(\hat{\rho}A^{\eta\eta})^n\bar{\delta}_\eta] \times [I-2h(\hat{\rho}A^{\xi\zeta})^n_{l+1/2}\Delta_\zeta]\,(\phi^{n+1}-\phi^n) = h\omega\{\bar{\delta}_\xi(\hat{\rho}U)^n + \bar{\delta}_\eta(\hat{\rho}V)^n + 2(\hat{\rho}W)^n_{l+1/2} + \tfrac{1}{4}\Delta_\zeta[\bar{\delta}_\xi(\hat{\rho}U^n) + \bar{\delta}_\eta(\hat{\rho}V^n)]\} \tag{35}$$

Equation (35) is of the same form as Eq. (25); hence, tangency can be enforced implicitly in the ADI algorithm given by Eqs. (28) with the tridiagonal and right-hand-side terms modified appropriately.

Results and Discussion

The three-dimensional dual-potential procedure outlined above has been used to simulate the flow through the 80 × 120 ft leg of the NFAC at the Ames Research Center. The results are compared to experimental data taken on a 1/15-scale model of the 80 × 120 ft leg. Screens and vanes are placed at the entrance of the inlet to isolate the test section from outside winds. Also, the screens prevent birds and other objects from entering the tunnel. The presence of these screens and vanes is accounted for in the numerical simulation as a jump condition based on actuator disk theory. The contraction ratio for the tunnel is 5:1, and the test section Mach number was taken to be 0.15.

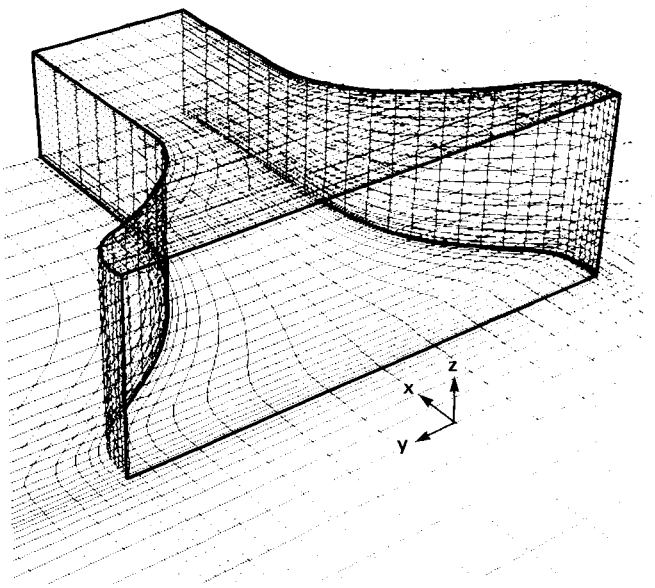

Fig. 2 Perspective view of the grid for the NFAC inlet model showing the ground plane and tunnel walls.

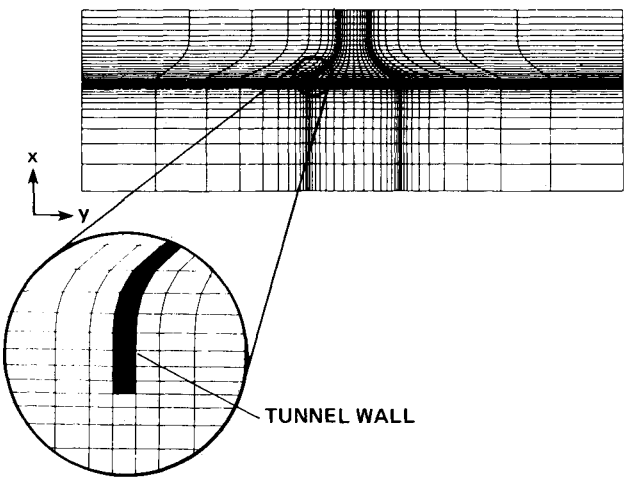

Fig. 3 Sheared grid for the 80 × 120 ft leg of the NFAC in the *x-y* plane at midheight.

A three-dimensional grid to model the 80 × 120 ft leg of the NFAC was generated using simple algebraic shearing. A perspective view of the tunnel walls and floor and the orientation of the coordinate axes is shown in Fig. 2. The origin of the coordinate system is located at the center of the inlet entrance. The grid represents the NFAC accurately, except for the rounded lip at the entrance of the inlet. To avoid a complex grid generation task, the rounded lip was not modeled. Since the 80 × 120 ft wind tunnel rests on the ground, the grid and the boundary conditions must model the ground plane for the correct inflow conditions to be obtained. The computational domain includes the wind tunnel and its surrounding region to facilitate the application of boundary conditions in the far field. All calculations were performed on a 39 × 41 × 34 grid, of which 26 × 17 × 21 grid points are interior to the wind tunnel. The tunnel walls are modeled to have a thickness equal to a single grid increment. The actuator disk modeling the screens and/or vanes is located at a ξ = constant plane corre-

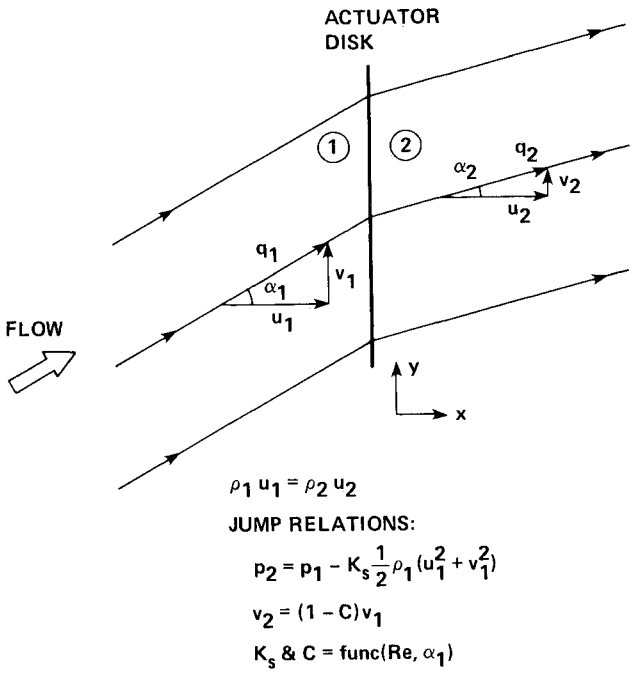

Fig. 4 Deflection of flow through an actuator disk model for a screen.

sponding to the location of the trailing edge of the vanes in the actual configuration. Figure 3 shows the grid in the x-y plane at midheight of the tunnel. A detail of the grid is given in Fig. 3 to illustrate the modeling of the tunnel walls. The average width of the test section, 100 ft, was chosen as the reference length in the calculations, and all results are presented accordingly.

The flow is assumed to be irrotational outside of the tunnel, and only the potential function ϕ needs to be computed there. Upstream and in the far field, the value of the potential is kept constant at its freestream value. At outflow, outside the tunnel, the streamwise component of velocity is allowed to vary by using a zero-gradient boundary condition on U. Tangency is enforced at the ground plane and at all the tunnel walls (interior and exterior) through the implicit boundary conditions on ϕ described earlier. The flow rate through the tunnel is determined by specifying the axial velocity ϕ_x in the test section. On each tunnel wall, the vector potential corresponding to the near-normal direction to the surface is obtained from its consistency relation, and the other two vector potential functions are kept constant. For example, on the ground plane ζ = constant, ϑ and χ are set to zero, and ψ is obtained from Eq. (22). At the outflow boundary ξ = constant, χ and ψ are obtained using a second-order extrapolation technique, whereas ϑ is computed from the vector potential consistency relation.

In the absence of any screens and/or vanes, the entire flow is assumed irrotational; hence, only ϕ needs to computed, with the other variables being constant. With screens and vanes, a pressure loss across these devices sets up a rotational flowfield inside the tunnel, which is accounted for by solving for the entropy, vorticity, and the vector potential functions. It is necessary to solve for these variables only within the tunnel, since the flow upstream of the vanes and screens is taken to be irrotational. Inflow boundary conditions for entropy and the vector potential functions are obtained from the actuator disk model for the vanes and screens.

The presence of vanes and screens at the entrance of the wind-tunnel inlet is modeled using actuator disk theory,[10,11] in which these devices are idealized to a jump condition. Vanes and screens constrain the flow in some specified direction and produce a drag force opposing the motion of the fluid. The drag or resistance produced by vanes and screens can be expressed in terms of the pressure loss across the actuator disk model. For a given screen or vane, the pressure drop can be em pirically determined as a function of the local dynamic head as

$$p_2 = p_1 - K\tfrac{1}{2}\rho_1 q_1^2 \tag{36}$$

Here, p is the pressure, and the subscripts 1 and 2 refer to locations immediately upstream and downstream of the actuator disk, as indicated in Fig. 4. This pressure drop across the actuator disk is related to the entropy jump across the disk as

$$\frac{s_2 - s_1}{R} = \frac{\gamma}{\gamma - 1} \ln \frac{T_2}{T_1} - \ln \frac{p_2}{p_1} \tag{37}$$

The loss coefficient K, which appears in Eq. (36), is empirically determined as a function of the local Reynolds number, onset flow angle, and the geometric characteristics of the screens and vanes. The contribution to the loss coefficient from the vanes and the screens may be separated into two components as

$$K = K_v + K_s \tag{38}$$

where K_v denotes the vane-loss coefficient and K_s the screen-loss coefficient.

In addition to creating a drag force, a screen turns the flow passing through it. At a given Reynolds number, the change in the tangent of the flow angle is found to be a function of the upstream flow angle.[10] This corresponds to a change in the lateral component of velocity ($\rho_1 u_1 = \rho_2 u_2$ for screens aligned normal to the x axis), and, for onset flow angles up to 40 deg, this change is found to be proportional to the upstream lateral velocity, i.e.,

$$u_1 \tan\alpha_1 - u_1 \tan\alpha_2 = C u_1 \tan\alpha_1 \tag{39}$$

where $u \tan\alpha = (v^2 + w^2)^{1/2}$ is the lateral component of velocity. A further simplification is achieved by assuming that Eq. (39) is valid for the individual components of lateral velocity v and w. The cascade of vanes at the entrance of the test section also directs the flow at a specified angle, thereby determining the y component of velocity as

$$v_2 = u_2 \tan\theta \tag{40}$$

where θ is the splay, or turning, angle of the vanes. A proper distribution of the splay angle can minimize the variation of total pressure in the test section.[11]

The coefficients K_v, K_s, and C used in this study are based on the experimental data of Refs. 11 and 12. Except for one case (Fig. 8), values of $K_s = 1.8$, $K_v = 0.4$, and $C = 0.2$ were used in the numerical simulations. Further details of the actuator disk model for the screens and vanes and its implementation in the numerical simulation can be found in Ref. 13.

As a simple verification of the numerical procedure, Figs. 5 and 6 show solutions obtained for potential flow alone ($K = 0$) and comparisons with other available data as taken from Ref. 14. The experimental results presented throughout were obtained from a 1/15-scale model of the NFAC. Figure 5 shows the variation of the pressure coefficient, $Cp = (p - p_t)/\frac{1}{2}(\rho u^2)_t$, along the side wall at midheight of the tunnel. Here, the subscript t refers to the test section, which is at the outflow boundary in the present simulation. Experimental data taken at 3.5 ft above midheight of the tunnel and results from an Euler calculation[14] at 4.2 ft above midheight of the tunnel are also plotted in this figure (the total height of the test section is 80 ft). The spike in the present results is attributed to the simplified treatment of the lip. In the present calculation, the flow rate was fixed by prescribing ϕ_x, whereas, in the Euler method, a nonreflecting boundary condition on pressure was

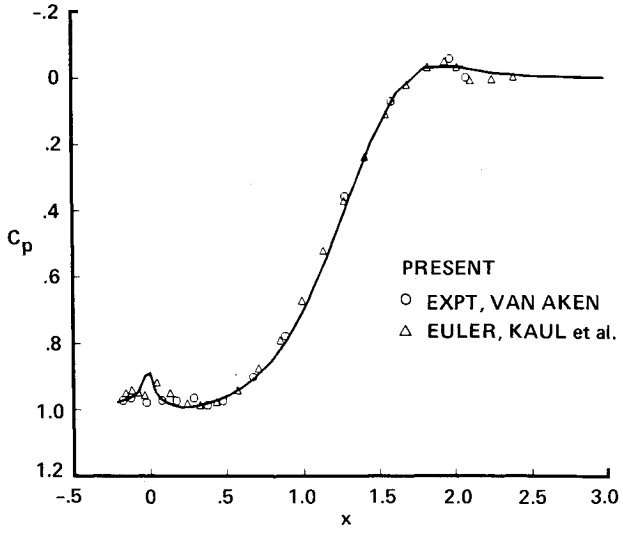

Fig. 5 Variation of pressure coefficient with length along a side wall at midheight of the tunnel.

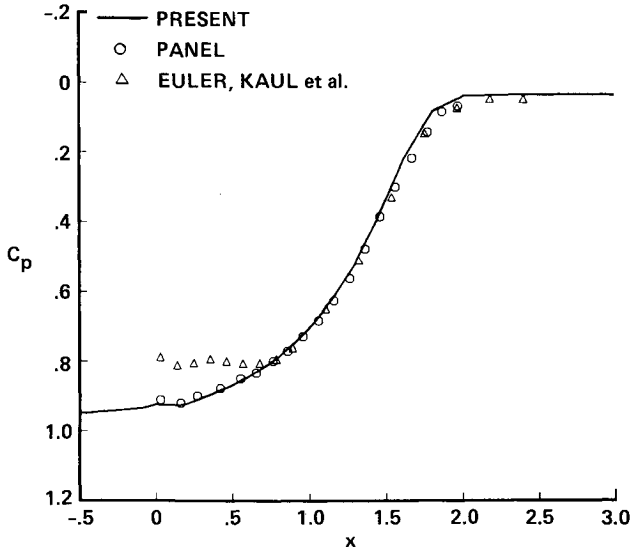

Fig. 6 Variation of pressure coefficient with length on the tunnel floor at midspan.

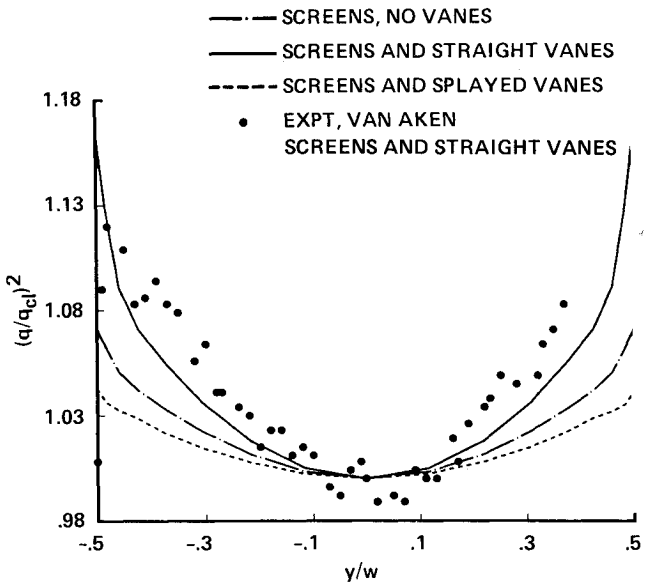

Fig. 7 Variation of dynamic pressure in the test section with span at midheight; $K_s = 1.6, K_v = 0.396$.

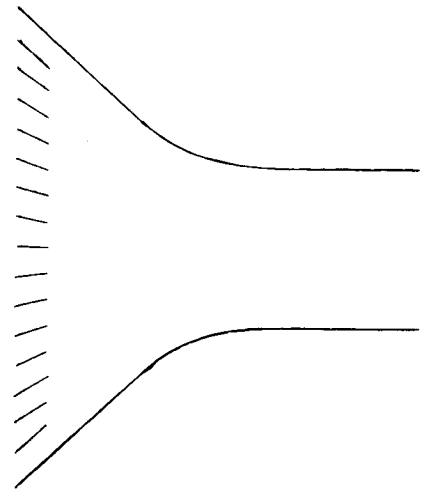

Fig. 8 A schematic view of the redesigned NFAC inlet.

used and the test section Mach number was fixed. Figure 6 shows a comparison of the pressure coefficient along the center of the tunnel floor, with Euler and panel method results taken from Ref. 14. It should be noted that the panel and Euler results are not at the center of the tunnel floor but 5 and 7 ft off of the midspan, respectively, and the width of the test section is 120 ft. The present calculations required about 5 μs per iteration per grid point on a Cray XMP vector processor, and fully converged results were obtained in 900 iterations, which correspond to about 240 s of cpu time.

In the design of wind tunnels, it is, of course, essential to maintain uniform flow in the test section, and screens and vanes (located upstream of the test section) are frequently used to improve the flow quality in the test section and isolate the wind tunnel from external turbulence. However, these devices induce a pressure loss that varies with the upstream dynamic pressure. If they are placed in a region with substantial variation of upstream velocity, they can induce a significant pressure variation (and therefore rotational flow) that can persist far downstream. Placing a screen in the wind-tunnel inlet can therefore induce an undesirable nonuniform flow in the test section. This effect is demonstrated in Fig. 7 for the original NFAC inlet; the figure shows the variation of the dynamic pressure in the test section with the spanwise distance y/w at midheight corresponding to $z/h = 0$, where w is the width and h is the height of the test section. The quantity plotted in this figure is the normalized dynamic pressure, $(q/q_{cl})^2$, where the subscript cl refers to the centerline. Three numerical results are shown in the figure corresponding to actuator disk models for screens alone, screens and straight vanes, and screens and splayed vanes. In one case, the vanes are straight; i.e., they are aligned with the axis of the tunnel [$\theta = 0$ in Eq. (40)], just as in the original NFAC design. In the other case, the vanes are splayed at angles developed for the redesigned NFAC.[11,12] Along with the numerical results, experimental data from a 1/15-scale model with straight vanes[12] are also plotted in this figure. The agreement with experiment is relatively good and indicates that the original inlet configuration results in an unacceptably high variation of flow quality in the test section.

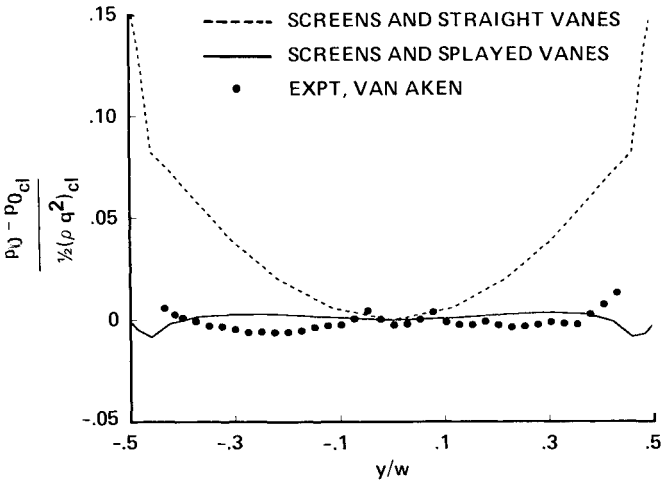

Fig. 9 Variation of total pressure coefficient in the test section with spanwise distance at midheight.

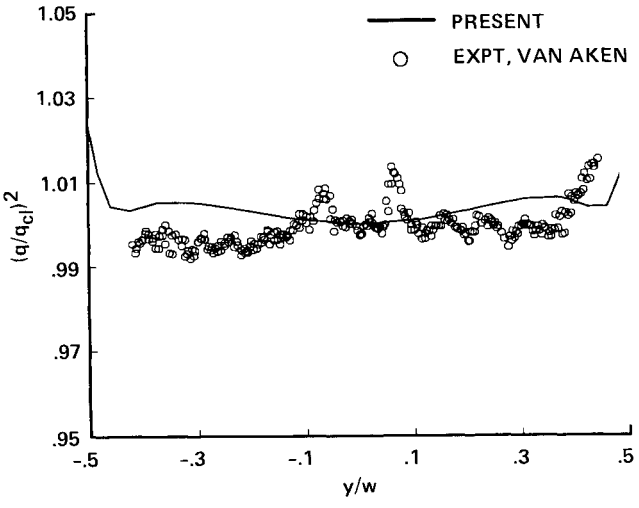

Fig. 10 Spanwise variation of dynamic pressure in the test section at $z/h = 0.166$ (splayed vanes).

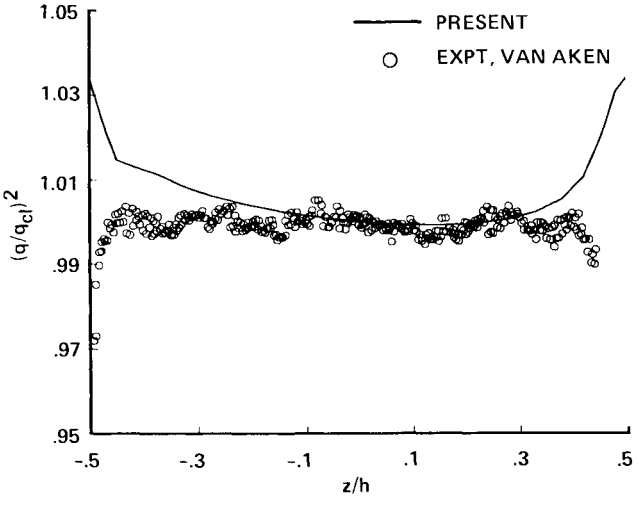

Fig. 11 Variation of dynamic pressure with height in the test section at $y/w = 0.375$ (splayed vanes).

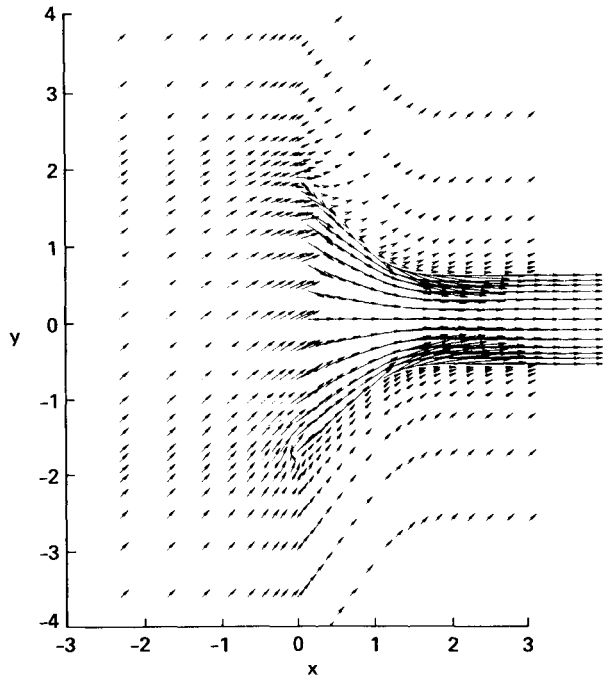

Fig. 12 Plot of velocity vectors for wind blowing at 45 deg at midheight (splayed vanes).

A numerical and experimental study of the NFAC[11] resulted in a slight modification to the inlet geometry. The curved walls in the span (or y direction) were replaced with straight walls near the entrance of the inlet, and the vanes were splayed at angles that are close to the "ideal" streamline angles at the entrance of the inlet. A schematic view of this new configuration is shown in Fig. 8; again, the true lip geometry is not represented. Results obtained for this modified tunnel are shown in Figs. 9–11. Also shown in these figures are experimental data from a 1/15-scale model.[12] Figure 9 shows the variation of the total pressure coefficient $(p_0 - p_{0_{cl}})/\frac{1}{2}(\rho q^2)_{cl}$, with spanwise distance at midheight of the test section ($p_0 = p + \frac{1}{2}\rho q^2$). Again, two splay distributions were examined: zero splay angles and the redesigned splay distribution. The results show a dramatic improvement in test-section flow quality for the case of splay distribution, and the agreement with experiment is good except near the walls. This is perhaps expected because viscous effects are not taken into account in the present procedure, and the correct lip geometry is not modeled. Figures 10 and 11 compare predictions with measurements of the dynamic pressure at two different height and span locations, respectively, in the test section. Overall, the agreement with experiment is satisfactory, except near the walls.

The preceding calculations were performed with zero freestream velocity, i.e., with no wind outside the tunnel. With the present code, a variety of outside wind conditions can be simulated by changing the far-field boundary conditions on ϕ (including rotational incoming flow if the vector potential functions are solved there). The effect of wind direction on the test-section flow quality was studied by simulating a case in which the wind velocity was about 15% of the test-section velocity and blowing at an angle of 45 deg with respect to the axis of the tunnel. Figure 12 shows the velocity vectors in a horizontal plane at midheight. Figure 13 shows the spanwise variation of dynamic pressure at midheight, along with results for the case in which the wind was blowing at 0 deg. The results indicate that the vanes, inlet length, and screens do a relatively good job of isolating the test section from such extreme variation in external flow conditions. This has been confirmed experimentally, though quantitative data are not available for comparison.

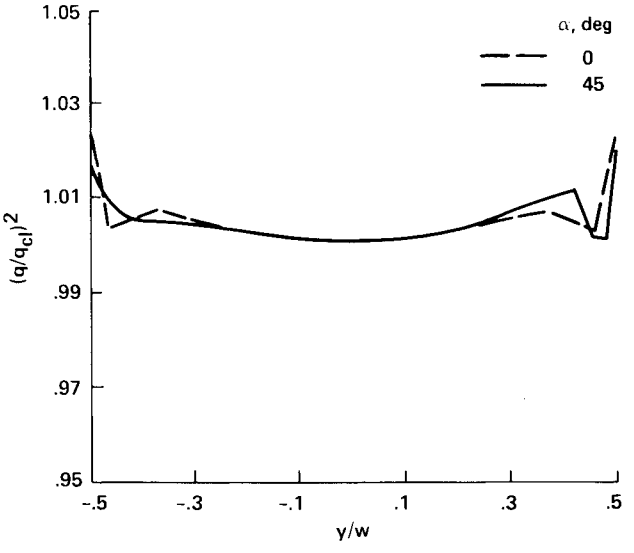

Fig. 13 Effect of wind direction on dynamic pressure in the test section at midheight (splayed vanes).

Concluding Remarks

A finite-difference procedure has been developed for solving the steady form of the Euler equations in three dimensions using the dual-potential velocity decomposition. The procedure has been shown to be useful in predicting the flow through indraft wind tunnels, including the effects of screens and vanes. Although the exact geometry and viscous boundary-layer effects are not modeled, the solutions are in satisfactory agreement with experimental and other numerical results.

Acknowledgments

The authors acknowledge Rimon Arieli and Neal Chaderjian, who contributed to the formulation and initial coding of the dual potential numerical algorithm, and thank William Van Dalsem and James Ross for many helpful discussions. Financial support for the Iowa State University authors was provided by NASA University Consortium Grant NCA2-17.

References

[1]Chaderjian, N. M., "The Numerical Simulation of Steady Transonic Rotational Flow Using a Dual Potential Formulation," Ph.D. Dissertation, Stanford University, Stanford, CA, 1984.

[2]Chaderjian, N. M. and Steger, J. L., "The Numerical Simulation of Steady Transonic Rotational Flow Using a Dual Potential Formulation," AIAA Paper 85-0368, Jan. 1985.

[3]Hirasaki, G. J. and Hellums, J. D., "Boundary Conditions on the Vector and Scalar Potentials in Viscous Three-Dimensional Hydrodynamics," *Quarterly of Applied Mathematics,* Vol. 28, July 1970, pp. 293-296.

[4]Wong, A. K. and Reizes, J. A., "An Effective Vorticity-Vector Potential Formulation for the Numerical Solution of Three-Dimensional Duct Flow Problems," *Journal of Computational Physics,* Vol. 55, July 1984, pp. 98-114.

[5]Chaviaropoulos, P. Giannakoglou, K., and Papailiou, K. D., "Numerical Computation of Three-Dimensional Rotational Inviscid Subsonic Flows, Using the Decomposition of the Flow Field Into a Potential and a Rotational Part," American Society of Mechanical Engineers Paper 86-GT-169, June 1986.

[6]Davis, R. L., Carter, J. E., and Hafez, M., "Three-Dimensional Viscous Flow Solutions With a Vorticity-Stream Function Formulation," AIAA Paper 87-0601, Jan. 1987.

[7]Panton, R. L., *Incompressible Fluid Flow,* Academic, New York, 1984, pp. 313-314.

[8]Bridgeman, J. O., Steger, J. L., and Caradonna, F. X., "A Conservative Finite Difference Algorithm for the Unsteady Transonic Potential Equation in Generalized Coordinates," AIAA Paper 82-1388, Aug. 1982.

[9]Ballhaus, W. F., Jameson, A., and Albert, J., "Implicit Approximate Factorization Schemes for the Efficient Solution of Steady Transonic Flow Problems," *AIAA Journal,* Vol. 16, June 1978, pp. 573-579.

[10]Horlock, J. H., *Actuator Disk Theory,* McGraw-Hill, London, 1978, pp. 12-75.

[11]Ross, J. C., Olsen, L. E., Meyn, L. A., and Van Aken, J. M., "A New Design Concept for Indraft Wind-Tunnel Inlets with Application to the National Full-Scale Aerodynamics Complex," AIAA Paper 86-0043, Jan. 1986.

[12]Van Aken, J. M., "Experimental Investigation of Several Inlet Flow Cascades for the NFAC 80- by 120-Foot Indraft Wind Tunnel," Univ. of Kansas Center for Research, Inc., Lawrence, KS, KU-CRINC Rept. 6900-2, 1986.

[13]Rao, K. V., "A Three-Dimensional Dual Potential Procedure for Rotational Flows," Ph.D. Dissertation, Iowa State Univ., Ames, IA, 1987.

[14]Kaul, U. K., Ross, J. C., and Jacocks, J. L., "A Numerical Simulation of the NFAC (National Full-Scale Aerodynamics Complex) Open-Return Wind Tunnel Inlet Flow," AIAA Paper 85-0437, Jan. 1985.